Accepted Manuscript

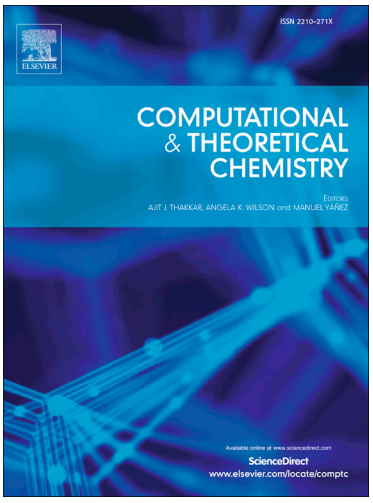

Multireference Equation of Motion Coupled Cluster Benchmark Study of Magnetic Model Systems

Siyuan Wu, Johnathan Steffen, Piaoyu Hu, Marcel Nooijen

PII: S2210-271X(18)30091-4
DOI: https://doi.org/10.1016/j.comptc.2018.03.009
Reference: COMPTC 2743

To appear in: *Computational & Theoretical Chemistry*

Received Date: 10 January 2018
Accepted Date: 13 March 2018

Please cite this article as: S. Wu, J. Steffen, P. Hu, M. Nooijen, Multireference Equation of Motion Coupled Cluster Benchmark Study of Magnetic Model Systems, *Computational & Theoretical Chemistry* (2018), doi: https://doi.org/10.1016/j.comptc.2018.03.009

Multireference Equation of Motion Coupled Cluster Benchmark Study of Magnetic Model Systems

Siyuan Wu, Johnathan Steffen, Piaoyu Hu, Marcel Nooijen[1]

Department of Chemistry, University of Waterloo, 200 University Avenue West, Waterloo, Ontario N2L 3G1, Canada

Abstract

The multireference equation of motion coupled cluster (MREOM-CC) approach including spin-orbit coupling is applied to magnetic model systems FArO, FArOF and FArFOH, and compared to benchmark multireference Configuration Interaction (MRCI) approaches in the case of FArO. In the MREOM calculations, convenient high-spin states provide reference reduced density matrices, that are used to obtain a sequence of similarity transformations of the Hamiltonian. All low-lying magnetic states are obtained subsequently from a compact diagonalization of the transformed Hamiltonian. The accuracy of MREOM is shown to be comparable to MRCI+Q, but the approach is significantly more efficient for systems with a large number of electronic states. Moreover, MREOM is nearly size-consistent and this allows one to perform meaningful calculations of the strength of the magnetic coupling in the weak coupling limit.

Keywords: multireference, equation of motion, coupled cluster, magnetic model systems.

1. Introduction

Human knowledge of magnetic phenomena has a very long history, going back to ancient times [1]. Today, the quantum mechanical description of magnetic phenomena is well understood, but the first principle calculations of magnetic properties is still a challenge [2]. A convenient approach to the problem is the construction of a model magnetic Hamiltonian [3, 4], and the extraction of the parameters that enter the Hamiltonian from first principle quantum chemistry approaches (e.g., see refs. [5, 6]). These approaches are well established, and have been reviewed, for example,

Email address: nooijen@uwaterloo.ca (Marcel Nooijen)
[1]Corresponding author

in refs. [2, 7]. The choice of quantum chemistry approach is delicate. Broken symmetry density functional theory (DFT) [8, 9] has been used extensively in the past [10, 11, 12, 13, 14], and has the virtue that the approach is efficient, but it also heavily relies on the assumed validity of the model Hamiltonian, and further underlying assumptions. A more satisfactory approach would be based on accurate wave function techniques that are suitable for strongly correlated systems. A method that has created significant interest is the Difference Dedicated Configuration Interaction (DDCI) approach [15, 16, 17, 18]. However, this method is expensive, using a large CI expansion, and in particular uses a threshold to screen configurations. Therefore, the method is somewhat delicate to apply. A clear alternative would be the internally contracted multireference Configuration Interaction (IC-MRCI) approach [19, 20]. However, this approach can also be expensive and it requires a balanced treatment of many low-lying electronic states.

In this work we consider the applicability of the newly developed multireference equation of motion coupled cluster (MREOM-CC) approach [21, 22, 23]. This methodology has clear advantages for magnetic systems. In the context of MREOM, one often starts with a state-averaged complete active space self-consistent field (CASSCF) calculation[24] and in the case of magnetic systems this CASSCF calculation can simply comprise the high-spin states in the system, which can usually be described using a small number of configurations. In addition, the choice of active orbitals is elementary for magnetic systems. In subsequent steps, a number of similarity transformations of the Hamiltonian are obtained, solving for the amplitudes along the way. To calculate the similarity transforms, one only requires the one and two-body reduced density matrices corresponding to the state-averaged complete active space (CAS). In the final step of MREOM, the transformed Hamiltonian is diagonalized over CAS, 1h and 1p configurations. The dimension of the final diagonalization space is very compact and one can obtain all low-lying magnetic states of interest in this final diagonalization step, in particular also low-spin states. Because the final diagonalization space is small, it is feasible to calculate systems with a sizeable number of magnetic atoms. Moreover, the MREOM implementation in ORCA [25, 26, 27] provides a treatment of spin-orbit coupling (SOC) [28].

The purpose of this paper is to determine the accuracy of MREOM including SOC for magnetic systems. To do this, we design artificial magnetic systems that are fairly easy to compute, and we can compare MREOM results to benchmark MRCI+Q, both including a treatment of SOC. The artificial magnetic systems consist of open-shell atoms like F, O or H and a closed-shell Ar atom.

Magnetic atoms are interacting with each other, while Ar atom acts like a bridge in the magnetic system and accounts for so-called super-exchange [29, 30, 31]. These systems represent significant complexity as the occupation of spatial orbitals may differ between low-lying states. This is due to the use of spatially degenerate atoms. It will be demonstrated that SOC_MREOM results follow SOC_MRCI+Q results quite closely, while in addition the MREOM results are size-consistent for all practical purposes. This paper is organized as follows. In section 2, we discuss the underlying theory of MREOM and the mean-field treatment of SOC. In section 3, computational details regarding some variants of MREOM, and the details concerning the MRCI calculation in Molpro [32] are discussed. In section 4, we provide in depth comparisons for the simple FArO model system, and we discuss a modification to the default spin-orbit mean-field method in ORCA to maintain size-consistency. MREOM is then applied to magnetic systems that have up to four magnetic sites to establish the promise of the method.

2. Theory

The MREOM-CC approach [21, 22, 23] provides a convenient way to calculate a large number of electronic excited states using an efficient transform and diagonalize strategy. The starting point of an MREOM calculation is a state-averaged CASSCF calculation, where all states of interest are considered to be qualitatively well described by linear combination of electronic configurations which comprise the CAS. Let us denote i', j', k', l' as inactive core orbitals, w, x, y, z, as active orbitals, i, j, k, l as occupied orbitals, which can be either inactive or active, a, b, c, d, as virtual orbitals, p, q, r, s, as general orbitals. The key idea of MREOM methodology is that a sequence of many-body similarity transformations are applied to the second-quantized Hamiltonian. In general, many body transformations with respect to Kutzelnigg-Mukherjee normal ordering [33, 34, 35], can be expressed as follow:

$$\begin{aligned}
&\hat{G} = \left\{e^{\hat{Y}}\right\}^{-1} \hat{H}\left\{e^{\hat{Y}}\right\} \rightarrow \left\{e^{\hat{Y}}\right\}\hat{G} = \hat{H}\left\{e^{\hat{Y}}\right\} \rightarrow, \\
&\hat{G} = (\hat{H}\left\{e^{\hat{Y}}\right\})_{Connected} - (\left\{e^{\hat{Y}} - 1\right\}\hat{G})_{Connected} = ... \\
&\quad = g_0 + g^p_r\{p^\dagger r\} + \frac{1}{4} g^{pq}_{rs}\{p^\dagger r q^\dagger s\} + \cdots . \qquad (1)
\end{aligned}$$

A key observation is that such a transformed Hamiltonian is explicitly a connected operator if $\hat{Y}$ is connected, which is the case in MREOM.

In this work, we will describe a sequence of transformations which has been implemented in the ORCA package, and which in full is referred to as the MR-EOM-T|T†|SXD|U method. We will consider the implementation of operators $\hat{T}, \hat{S}, \hat{X}, \hat{D}, \hat{U}$ in terms of similarity transformations. Below, we use the Einstein summation convention meaning that repeated indices are always summed over.

The excitation operator $\hat{T}$ expressed in terms of the single and double spin-free generators of the unitary group $\hat{E}^q_p$ and $\hat{E}^{rs}_{pq}$ is given by

$$\hat{T} = \hat{T}_1 + \hat{T}_2 = t^i_a \hat{E}^a_i + \frac{1}{2} t^{ij}_{ab} \hat{E}^{ab}_{ij}, \tag{2}$$

where t^i_a and t^{ij}_{ab} are single and double excitation amplitudes, respectively. The $\hat{T}$-operators account for excitations from occupied orbitals (core or active) to virtual orbitals. These operators all commute and the exponential excitation operator is given by $e^{\hat{T}}$.

The Hamiltonian $\hat{H}$ is expressed in the usual second-quantized form, and the first transformation in MREOM is obtained as

$$\begin{aligned} \hat{\bar{H}} &= e^{-\hat{T}} \hat{H} e^{\hat{T}} \\ &= \bar{h}_0 + \bar{h}^p_q \left\{ \hat{E}^q_p \right\} + \bar{h}^{pq}_{rs} \left\{ \hat{E}^{rs}_{pq} \right\} + \bar{h}^{pqr}_{stu} \left\{ \hat{E}^{stu}_{pqr} \right\} + \cdots , \end{aligned} \tag{3}$$

noting that $e^{\hat{T}}$ is already in normal-ordered form.

The t-amplitudes are solved from [36, 23]

$$\sum_k \omega_k \langle R_k | E^i_a \hat{\bar{H}} | R_k \rangle = 0, \tag{4}$$

$$\bar{h}^{ab}_{ij} = 0 \tag{5}$$

where $|R_k\rangle$ refers to states obtained from the state-averaged CASSCF and ω_k is the corresponding state weight.

The second transformation in the MR-EOM-T|T†|SXD|U scheme [26] is written as

$$\begin{aligned}\hat{\tilde{\mathcal{H}}} &= e^{\hat{T}^\dagger}\hat{\tilde{H}}_2 e^{-\hat{T}^\dagger} \\ &= \tilde{h}_0 + \tilde{h}^q_p\left\{\hat{E}^p_q\right\} + \tilde{h}^{rs}_{pq}\left\{\hat{E}^{pq}_{rs}\right\} + \tilde{h}^{stu}_{pqr}\left\{\hat{E}^{pqr}_{stu}\right\} + \cdots,\end{aligned} \tag{6}$$

in which $\hat{\tilde{H}}_2$ is the similarity transformed Hamiltonian in Eq. (3), truncated up to two-body operators. The de-excitation operator $\hat{T}^\dagger$ is defined as

$$\hat{T}^\dagger = t^a_i \hat{E}^i_a + \frac{1}{2} t^{ab}_{ij}\hat{E}^{ij}_{ab}, \tag{7}$$

and the de-excitation amplitudes are assumed to be the same as the excitation amplitudes

$$t^a_i \approx t^i_a, \tag{8}$$

$$t^{ab}_{ij} \approx t^{ij}_{ab}. \tag{9}$$

The similarity transformation of Eq. (6) is performed to make the Hamiltonian $\hat{\tilde{\mathcal{H}}}$ approximately Hermitian.

The third transformation takes the form

$$\bar{F} = \left\{e^{\hat{S}_2+\hat{X}+\hat{D}}\right\}^{-1}\hat{\tilde{\mathcal{H}}}_2\left\{e^{\hat{S}_2+\hat{X}+\hat{D}}\right\}, \tag{10}$$

in which $\hat{\tilde{\mathcal{H}}}_2$ include the zero-, one- and two-body elements of $\hat{\tilde{\mathcal{H}}}$ in Eq. (6). Here the $\hat{S}_2, \hat{X}$ and $\hat{D}$ operators are defined as

$$\hat{S}_2 = s^{ax}_{i'j'}\hat{E}^{i'j'}_{ax}, \tag{11}$$

$$\hat{X} = \hat{X}_2 = x^{ay}_{xj'}\hat{E}^{xj'}_{ay}, \tag{12}$$

$$\hat{D} = \hat{D}_2 = d^{ay}_{i'x}\hat{E}^{i'x}_{ay}. \tag{13}$$

The operator $\hat{S}_2$ describes excitation operators that excite from two core orbitals into an active and a virtual orbital. The $\hat{X}$ and $\hat{D}$ operators are semi-internal excitations in which an electron

in a core orbital is excited to a virtual orbital, while in addition a one-orbital replacement is done in active space. In the 'diagonal' $\hat{D}$ operator, orbitals a and i' describing a core-particle excitation have the same spin, while in the exchange-type $\hat{X}$ operator, labels a and j' can have different spin. These operators do not commute and use of normal-ordered exponential is convenient.
The SXD-amplitudes are solved from

$$f^{ax}_{i'j'} = f^{ay}_{xj'} = f^{ay}_{i'x} = 0. \tag{14}$$

In all above expressions, we only retain terms that are at most quadratic in the cluster amplitudes [22].

The final similarity transformation of the MR-EOM-T|T†|SXD|U approach is given by

$$\begin{aligned}\hat{G} &= e^{-\hat{U}}\hat{F}_2 e^{\hat{U}} \\ &= g_0 + g^p_q\left\{\hat{E}^q_p\right\} + g^{pq}_{rs}\left\{\hat{E}^{rs}_{pq}\right\} + g^{pqr}_{stu}\left\{\hat{E}^{stu}_{pqr}\right\} + \cdots,\end{aligned} \tag{15}$$

where $\hat{F}_2$ indicates that $\hat{F}$ in Eq. (10) has been truncated up to two-body operators. The operator $\hat{U}$ is defined as

$$\hat{U} = \hat{U}_2 = \frac{1}{2}u^{xy}_{i'j'}\hat{E}^{i'j'}_{xy}. \tag{16}$$

The operator $\hat{U}$ accounts for a double core to active excitation.
The U-amplitudes are solved from

$$g^{xy}_{i'j'} = 0. \tag{17}$$

Once again, we discard terms that are more than quadratic in the amplitudes. All MREOM amplitudes equations are expressed in terms of spatial state-averaged one-particle reduced density matrices, and the state-averaged two-body cumulant. The detailed equations have been derived using computer algebra, and a code generator is used to develop the computer code in ORCA, written in the C++ language [25, 26]. Upon transformation of the Hamiltonian using $\hat{T}, \hat{S}, \hat{X}, \hat{D}, \hat{U}$ almost all excitation components in the final $\hat{G}$ operator can no longer excite out of any CAS reference determinant. The only non-zero excitations that remain are of the types $\hat{E}^{xy}_{zi}$, which gives rise to 1-hole excitations, and $\hat{E}^{ax}_{zi}$ which couples to 1-particle excitations. For this reason, the final transformed Hamiltonian $\hat{G}$ is diagonalized over CAS, 1p and 1h excitations.

The inclusion of SOC has been discussed in previous studies [28, 37, 38]. A good starting point to introduce the SOC effect is that a number of I electronic states

$$|\Psi_I^{SS}\rangle = \sum_\mu C_{\mu I}|\Phi_\mu^{SS}\rangle \tag{18}$$

are obtained following the diagonalization of the similarity transformed Hamiltonian [26, 38]. For the inclusion of SOC effects, the functions $|\Psi_I^{SM}\rangle$ with spin projection number $M = -S, \cdots, S$ can be generated by the repeated application of spin shift operators on the states $|\Psi_I^{SS}\rangle$. The energies of basis states $|\Psi_I^{SM}\rangle$ treated by the quasi-degenerate perturbation theory (QDPT) can be obtained by

$$\langle\Psi_I^{SM}|\hat{G} + \hat{H}_{SOMF}|\Psi_J^{S'M'}\rangle = \delta_{IJ}\delta_{SS'}\delta_{MM'}E_I^{(S)} + \langle\Psi_I^{SM}|\hat{H}_{SOMF}|\Psi_J^{S'M'}\rangle, \tag{19}$$

where the spin-orbit mean-field (SOMF) operator is described in refs. [28, 39] and the calculation of the SOMF matrix elements is given in ref. [38]. In this formulation, it is crucial that the MREOM Hamiltonian $\hat{G}$ commutes with the spin operators. In addition, we use the bare $\hat{H}_{SOMF}$ rather than a transformed SOC operator. This is an approximation that has been shown to work fairly well for atoms [40].

3. Computational Details

The main strategy of MREOM methods for studying magnetic systems is that many electronic excited states can be obtained, while the preceding state-averaged CASSCF calculation is performed for only a few high-spin states. The amplitudes in MREOM are solved using state-averaged density matrices from the CASSCF calculation. As shown in Table 1, two variations of MREOM including the definition of final MRCI diagonalization space are discussed.

In this work, we employ both ORCA and Molpro quantum chemistry packages. The complete active space configuration interaction (CASCI) or CASSCF and MRCISD+Q [19, 20, 41, 42] approaches are performed to study the effect of dynamic correlation using the Molpro package. Two MREOM approaches listed in Table 1 are performed in ORCA to test the efficiency and the accuracy of the transform and diagonalize strategy. Moreover, DDCI3 and NEVPT2 [43, 44] approaches are also performed in ORCA for comparison purposes.

All calculations that include SOC are denoted as SOC_CASCI, SOC_MRCISD+Q, SOC_MREOM,

Method	Short name	Transformation(s)	Diagonalization space
MR-EOM-T|T†|SXD|U	MREOM	$\hat{T}_1 + \hat{T}_2 \vert \hat{T}_1^\dagger + \hat{T}_2^\dagger \vert \hat{S}_2 + \hat{X} + \hat{D} \vert \hat{U}$	CAS, 1p,1h
MR-EOM-T|T†|SXD-ph	MREOM_1p1h	$\hat{T}_1 + \hat{T}_2 \vert \hat{T}_1^\dagger + \hat{T}_2^\dagger \vert \hat{S}_2 + \hat{X} + \hat{D}$	CAS, 1p,1h, 2h, 1p1h

Table 1: The characteristics of the two MREOM approaches.

SOC_MREOM_1p1h, SOC_DDCI3 and SOC_NEVPT2, and are performed to understand the effect of SOC on magnetic systems. The default SOC approach in ORCA is defined as SOMF(1X), which has been discussed in ref. [28]. In this default approach, there is a tight threshold to include only states that are nearly degenerate with the ground state. This is not a good strategy for systems studied in this work (as will be shown later). Instead we use a modified SOMF(1X) approach denoted as m_SOMF(1X) in which the state-averaged density passed to the SOC program is obtained over *all states*. It is also important to note here that a full SOC_MRCISD+Q calculation in Molpro requires a lot of memory. Therefore, a lower level of accuracy approach is used in the Molpro package. The wavefunctions passed to the spin-orbit module in Molpro are generated by the MRCI with singles only, while the diagonal elements are replaced by precomputed MRCISD+Q energies.

Most calculations were performed using the cc-pVDZ basis set [45, 46], while a final comparison between MRCI and MREOM is done using the cc-pVTZ basis set [45, 46].

4. Results

4.1. Analysis of Results for the FArO System

Let us first introduce the FArO artificial magnetic system. The geometric structure of the system is given in Figure 1. To design a representative magnetic system, the distance between F, O and Ar is fairly large. Hence, the system essentially consists of the magnetic atoms F and O interacting with a spacer, while the atomic degeneracy is further lifted through interaction of F and O. The FArO system is chosen because it leads to a rich manifold of low-lying states. The low-lying state of the F-atom are $^2P_{\frac{1}{2}}$ and $^2P_{\frac{3}{2}}$ (6 states), while the oxygen atom has 9 low-lying states $^3P_0$, $^3P_1$ and $^3P_2$. Hence we anticipate 6x9 = 54 low-lying sates, that are perturbed from their non-interactive atomic nature through interaction with the Ar atom, and the additional complicated interaction (magnetic and spin-orbit) among the 54 electronic states. The distances between Ar-O and Ar-F are taken to be 2.9 Å. This distance is chosen, since this yields a fair splitting (of about 1200 cm^{-1}) between the lowest and highest state. The angle of 120° is chosen to enhance the direct magnetic interaction

between O and Ar atoms. Let us emphasize that the model is artificial, and is not expected to be feasible experimentally. The system is chosen as a small system that clearly illustrates the significant complexity of magnetic interactions and is suitable for benchmarking various electronic structure methods.

In this section, we first give a brief qualitative picture and analysis of such magnetic systems. In doing so, we have decided to look at the effect of the Argon atom, spin-orbit coupling, dynamical correlation and magnetic coupling. In addition, we report our analysis on testing the accuracy of the multireference methods performed in this work. Finally, we present some results on the analysis of FArO at various distances to investigate the importance of size-consistency of the electronic structure approaches.

4.1.1. Consideration of the Argon Atom and Spin-orbit Coupling

We start from a CASCI using the Molpro package to illustrate the effect of spin-orbit coupling and inclusion of the Ar atom on the statistical-mechanical properties analysis of the low-lying states of magnetic molecules. At first, CASCI and SOC_CASCI calculations have been performed for FArO and FXO at bond length R = 2.9 Å. In FXO, the Ar atom is replaced by auxiliary center such that F and O atoms are at the same positions as in FArO. Below, we more conveniently denote FXO as FO. To illustrate the results of the calculation in a convenient fashion, we draw a curve of excitation energy versus state number referred to as an excitation energy plot, and we also provide the heat capacity as a function of temperature. The heat capacity is obtained from a sum over states expression, that includes all low-lying magnetic states. Given each energy level E_n and temperature T, the thermal property is given by

$$Z = \sum_{n=0} e^{\frac{-(E_n - E_0)}{k_B T}} \tag{20}$$

$$P_n = \frac{1}{Z} e^{\frac{-(E_n - E_0)}{k_B T}} \tag{21}$$

$$U = \sum_n P_n E_n \tag{22}$$

$$C_v = \frac{1}{k_B T^2} \sum_n P_n (E_n - U)^2 \tag{23}$$

In Figure 2, we present a plot of excitation energies of FArO and FO for a total of 54 low-lying states. For the CASCI calculation of FO molecule, all low-lying excited states are located within

20 cm^{-1}. However, for the CASCI calculation of FArO molecule, the excitation energies for these low-lying states range from $0 \sim 600$ cm^{-1} with four basic energy splittings, which indicates that the excitation energies are sensitive to the inclusion of the Argon atom which acts as a spacer. The effect of the Ar atom is primarily that it breaks the symmetry of the atoms. This is illustrated in Table 2, where we list the energies for both ArF and ArO dimers. For ArF, the levels split in two groups. The p-orbital can be pointing along the ArF axis (P_z) or perpendicular to it (P_x, P_y). This leads to a 2+4 splitting for the ArF dimer. Likewise, for ArO, the p-orbitals are split into a parallel P_z and two perpendicular P_x, P_y orbitals, and the ^3P state for the oxygen atom splits into two groups due to 2 holes in the P_xP_y orbitals (3 states) and holes in P_xP_z or P_yP_z orbitals (6 states). Additional couplings occur due to spin-orbit coupling. In Table 2 we indicate the level splitting for ArO and ArF for a CASCI calculation both with and without spin-orbit coupling. The inclusion of dynamical correlation only slightly affects the major trend. When the Ar atom is absent, while also spin-orbit coupling is not included, only very small interaction between distant F and O atoms remain, as illustrated in Figure 2.

Molecule	Levels	Methods			
		CASCI	SOC_CASCI	SOC_MREOM	SOC_MRCISD+Q
ArF	1	0.0	0.0	0.0	0.0
	2	0.0	0.0	0.0	0.0
	3	205.9	157.2	199.6	195.0
	4	205.9	157.2	199.6	195.0
	5	205.9	484.2	504.2	505.9
	6	205.9	484.2	504.2	505.9
ArO	1	0.0	0.0	0.0	0.0
	2	0.0	0.0	0.0	0.0
	3	0.0	60.9	55.3	58.5
	4	0.0	60.9	55.3	58.5
	5	0.0	116.9	107.7	113.2
	6	0.0	150.3	130.8	140.6
	7	375.9	465.4	480.8	476.6
	8	375.9	465.4	480.8	476.6
	9	375.9	484.5	493.8	492.1

Table 2: Excitation energies for magnetic dimers ArF and ArO using the CASCI, SOC_CASCI, SOC_MREOM, SOC_MRCISD+Q. All results are in cm^{-1}

To test the effect of spin-orbit coupling, we also investigate the excitation energies and heat

capacity plots for FArO using CASCI and SOC_CASCI. In Figure 3, the excitation energies plot and heat capacity plot indicate that CASCI and SOC_CASCI calculations are quite different. In particular, the inclusion of SOC gives rise to a smearing of the energy levels. Moreover, the energy difference between the lowest and highest magnetic level increases significantly from 600 cm^{-1} to around 970 cm^{-1}. This indicates that the Argon atom and SOC are extremely important for the magnetic energy level spacing. This significant effect of spin-orbit coupling can already be seen for the dimer systems ArF and ArO.

4.1.2. Determination of the Effect of Dynamical Correlation

In the previous section, the qualitative performance based on the CAS level has been discussed. Those results support our motivation to explore this further in terms of the dynamical correlation contribution on the statistical-mechanical properties of the low-lying excited states. Here, we first report the performance of the SOC_CASCI and SOC_MRCISD + Q for FArO molecule at bond length R = 2.9 Å. In Figure 4, it is clear that the shapes of excitation energies plot and heat capacity plot are qualitatively similar, which indicates that the contribution from dynamic correlation is not large, but it is still important for quantitative accuracy. As has been discussed in ref. [2, 19, 20, 23], MRCISD+Q approach is considered to be fairly efficient but it is not rigorously size-consistent. MRCISD+Q method rapidly becomes expensive if the size of the molecule gets larger and in particular if the number of magnetic sites increase. DDCI3 approach also uses a large CI expansion and is expensive. NEVPT2 method employs a perturbative treatment which applies to CASSCF wavefunctions and is computationally efficient. MREOM approaches scale in a better way than MRCI+Q and DDCI3 and are applicable to larger systems because of the reduced final diagonalization space. As a result, it is of interest to make a comparison among the SOC_MRCISD + Q, SOC_MREOM, SOC_MREOM_1p1h, SOC_NEVPT2 and SOC_DDCI3 calculations. In Figure 5, the excitation energies plot and heat capacity plot for SOC_MREOM and SOC_MREOM_1p1h are seen to be closely comparable to those of SOC_MRCISD + Q and SOC_DDCI3 for the FArO molecule at R = 2.9 Å. This shows that MREOM approaches are convincingly accurate enough compared to MRCI+Q and DDCI3 approaches. In addition, from the excitation energies plot and heat capacity plot, NEVPT2 method is not comparable to the other four approaches. Also, the very slight difference between SOC_MREOM and SOC_MREOM_1p1h approaches indicates that the inclusion of the ph and 2h excitations is not significant. It is also interesting to note that in the heat

capacity plot of Figure 5, there is a visible peak below about $T = 5K$ for SOC_MRCISD + Q and SOC_DDCI3 approaches, which is not visible in the SOC_MREOM and SOC_MREOM_1p1h results. The low temperature behaviour of the heat capacity is shown more clearly in Figure 6. This peak arises because there are two low-lying excitation states sitting at 5 cm^{-1} for SOC_MRCISD + Q, and 2.9 cm^{-1} for SOC_DDCI3 calculation, while the two corresponding states energies are 0.3 cm^{-1} and 0.5 cm^{-1} for SOC_MREOM and SOC_MREOM_1p1h, respectively. This illustrates that such a small difference can have significant effects at low temperatures. From about $T = 20K$ onwards, all results except for SOC_NEVPT2 agree fairly well.

Here, we also indicate the computational costs between MRCI and MREOM calculations for FArO in Table 3. It is clear that MRCI method is significantly more expensive than MREOM-CC calculations even for small systems. Let us note that the MREOM implementation in ORCA only works in a serial fashion, while the Molpro MRCI calculations were run in parallel on 8 nodes.

Methods	cc-pVDZ	cc-pVTZ
SOC_MREOM	3m29s (1 node)	16m32s (1 node)
SOC_MREOM_1p1h	4m15s (1 node)	21m2s (1 node)
SOC_MRCISD+Q	7m34s (8 nodes)	45m18s (8 nodes)

Table 3: The comparison of computation timing (CPU time) between MRCI and MREOM methods for FArO using cc-pVDZ and cc-pVTZ basis sets. Each processor has a 12-core node and consists of Intel XEON 2.93 GHz CPUs with 12.3 MB of shared cache memory.

4.1.3. Consideration of the Magnetic Coupling Effect As a Function of Interatomic Distance: Size-consistency

From the results presented so far, it can be concluded that the Ar atom as well as atomic/dimeric spin-orbit coupling are mainly responsible for the splitting of the energy levels. The remaining splitting is due to the magnetic interactions between the states, mediated by the presence of the Ar atom. We would like to quantify these "true" many-body effects. To this end, we compare the total excitation energies (in cm^{-1}) of magnetic dimer FArO molecule with the sum of excitation energies of ArF and ArO magnetic monomer molecules for each corresponding low-lying excited state. Let us here define the two-body energy, which can be used to focus on the effects of magnetic

interactions. This can be expressed as

$$\Delta E_{\lambda\nu}^{two-body} = \Delta E_{\lambda\nu} - (\Delta E_{\lambda} + \Delta E_{\nu})$$

in which $\Delta E_{\lambda\nu}$ is the excitation energy of FArO, while ΔE_{λ} and ΔE_{ν} represent the corresponding excitation energies of ArF and ArO, respectively. The sum energies $(\Delta E_{\lambda} + \Delta E_{\nu})$ are sorted such that they correspond to magnetic excitation energies of FArO, $\Delta E_{\lambda\nu}$.

In Figure 7, the excitation energies plots show that the energy levels between interacting and non-interacting systems quite nearly match each other. This indicates that the true magnetic coupling effects in the model systems are small. The small two-body contribution to the excitation energies provide a stringent test of size-consistency. One would anticipate that these two-body energies show a rapid decay with the interatomic distance between ArO and ArF. Let us first check the results at CASCI level, and later consider dynamical correlation.

In Figure 8, we compare the two-body energies of FArO using the SOC_CASCI in both ORCA and Molpro package. A set of calculations containing 13 bond lengths ranging from 2.5 Å to 10 Å are performed to make a detailed comparison. The SOC_CASCI results in Molpro for the two-body interaction energies show the expected behaviour and rapidly and smoothly decay as a function of the ArO/ArF distance. Quite surprisingly, it is observed in Figure 8 that the default SOC approach denoted as SOMF(1X) in ORCA lacks of rigorous size-consistency as the asymptote does not go towards 0 cm^{-1}, for example for states 38 and 44. This issue with size-consistency in default ORCA SOC calculations using SOMF(1X) is due to the definition of the state-averaging. By default only states are included that are almost exactly degenerate. For FArO only one state is included, unless the distance is very large. However, for the linear molecules ArF and ArO, two states are included since the π states are doubly degenerate. This significantly affects SOC in the mean field approximation, and this causes the unexpected behavior. The solution to the problem for these particular systems is fairly straightforward: we include all 54 magnetic states in the definition of the average density that enters the SOMF(1X) procedure. An alternative procedure would be to use the states that are used in the high-spin CASSCF. This could be a most satisfactory general solution, but this requires a more substantial change to the ORCA code, and this is not pursued here. ORCA calculations are performed under m_SOMF(1X) again to test the size-consistency issue. In Figure 9, it can be seen that the size-consistency error in SOC_CASCI is fixed using the m_SOMF

(1X) approach. The above analysis indicates that the use of the two-body interaction energies as a function of nuclear geometry is a sensitive probe of proper size-consistency behaviour of the electronic structure methods considered. The smooth curve of each state as a function of geometry indicates that this partitioning of the excitation energies captures the physical phenomenon, and shows a clear strange behaviour when methods violate size-consistency, even if they do so in a mild manner. The above test is far more sensitive and instructive than a conventional analysis in terms of the difference in energy between non-interacting dimers, and we would not have identified the SOMF(1X) problem is ORCA in that way. In a further step, to test the size-consistency issue with inclusion of correlation energies, we perform SOC_MRCISD + Q and SOC_MREOM calculations on FArO molecule at the same 13 bond lengths. In all SOC_MREOM calculations reported in this paper (including previous section 4.1.2), we used the modified SOMF(1X) to include SOC. Figure 10 shows the behavior of two-body energies for states 40 and 47 as illustrative examples. As anticipated, the asymptote of MREOM approach is perfect at 0 cm^{-1}, as it is a nearly size-consistent method. One also observes that SOC_MRCISD + Q approach does not yield reasonable results, as the asymptote is not flat at 0 cm^{-1} at larger bond distances range. This clearly illustrates the violation of size-consistency. It strongly suggests that MRCI method is not suitable to examine magnetic coupling effects as a function of geometry.

4.2. Results for FArO using cc-pVTZ basis set

Here we present the results for FArO system at R = 2.9 Å using cc-pVTZ basis set. In Figure 11, the excitation energies plot and heat capacity plot for SOC_MREOM and SOC_MREOM_1p1h are closely comparable to those of SOC_MRCISD + Q. This illustrate the robustness of MREOM approach also for a larger basis set.

4.3. Results for Additional Model Systems

In this section, we first report the performance of the SOC_MRCISD+Q, SOC_MREOM, SOC_DDCI3 and SOC_DDCI3_b for NArOH molecule. The input cartesian coordinates of this molecule is given in Table 4. In Figure 12, it is interesting to note that the default SOC_DDCI3 method in ORCA is not comparable to SOC_MRCISD+Q and SOC_MREOM. The solution to this problem is to select more configurations in the CI space, which is labeled as SOC_DDCI3_b in Figure 12. It is clear that the excitation energies plot and heat capacity plot are then quite similar among SOC_MRCISD+Q,

SOC_MREOM and SOC_DDCI3_b.

In a further step, we will explore two larger artificial systems: FArOF and FArOFH. The

Z-matrix Symbol	Atomic Number	Coordinates		
		X	Y	Z
N	7	-2.28914901	0.85930980	-0.00000000
AR	18	-0.07917006	-0.51035914	-0.00000000
O	8	2.21198752	0.71870431	-0.00000000
H	1	-0.16034868	-3.10909153	0.00000000

Table 4: The cartesian coordinates of NArOH(Angstroms).

geometric structures of these two molecules are presented in Figure 13. The total number of low-lying excited states for FArOF and FArOFH is 324 and 648, respectively. Therefore, the SOC_MRCISD+Q calculation is quite expensive and is not available in this work. Instead, we perform the SOC_MREOM calculation of these magnetic molecules. The full SOC_MREOM calculation for FArOF and FArOFH takes about 2 CPU hours and 2 CPU days, respectively, on a single processor of a 12-core node, consisting of Intel XEON 2.93 GHz CPUs with 12.3 MB of shared cache memory. The excitation energies plot and heat capacity plot for FArOF and FArOFH are illustrated in Figure 14 and Figure 15, respectively.

5. Conclusion

In this work, we established the accuracy of the MR-EOM-T|T†|SXD|U approach implemented in the ORCA program, in conjunction with a modified SOMF(1X) inclusion of spin-orbit coupling for magnetic systems. The primary advantage of MREOM are the computational efficiency for systems that have many (hundreds of) electronic states, but which share the same active space. Magnetic systems can be considered as prototype examples to illustrate the merits of MREOM. Even though MREOM is not strictly size-consistent, in practice this is of no concern for systems of this type. The computational scaling of MREOM is not fundamentally different from MRCI, and one cannot push the methodology to a very large number of magnetic atoms. However, the method is sufficiently effective such that one can treat system with up to about four magnetic sites of arbitrary spin S. Therefore, one can treat magnetic coupling beyond two-body effects. In this paper, we have only tested the applicability of the approach for artificial model systems. A next step would be the application to more realistic models of magnetic materials, and the extraction

of magnetic model parameters along the lines discussed in ref. [2, 7]. Since magnetic systems are often fairly sizeable, and only a canonical version of MREOM has been implemented up to now, this requires a truncation of the molecular orbital basis, as considered before for transition metal compounds [25]. The application of MREOM to more realistic magnetic model systems will be considered in future work.

6. Acknowlegement

This research was supported by the National Science and Engineering Research Council (NSERC) of Canada through a discovery grant to M.N..

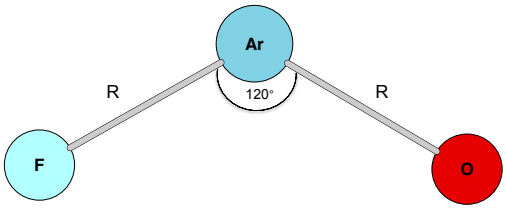

Figure 1: The geometric structure of the FArO system. R = r(Ar − F) = r(Ar − O), bond angle is 120°.

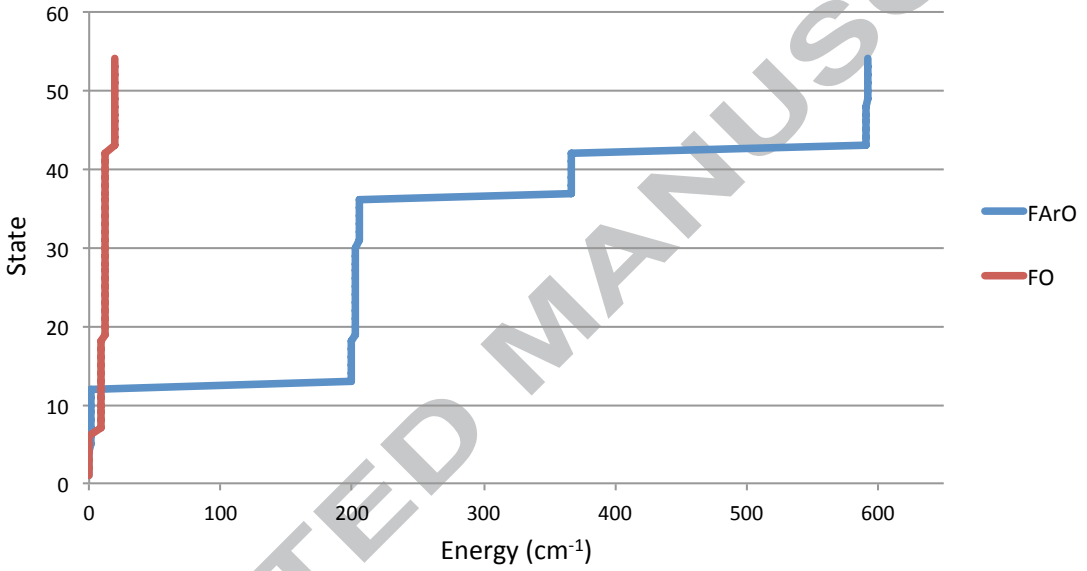

Figure 2: The excitation energies curve of FArO and FO molecules obtained using the CASCI.

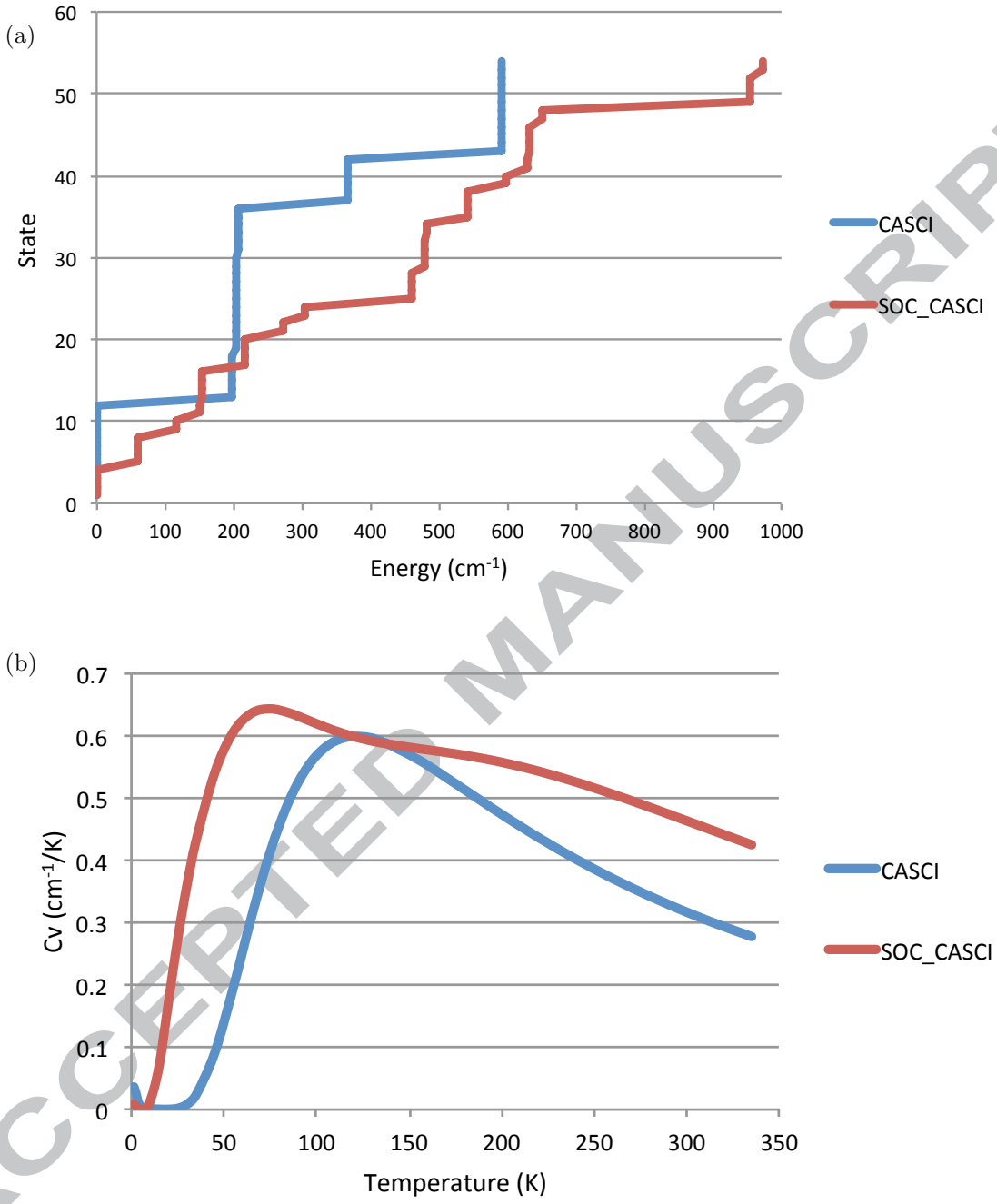

Figure 3: Plots of (a) excitation energies and (b) heat capacity for FArO using the CASCI and SOC_CASCI.

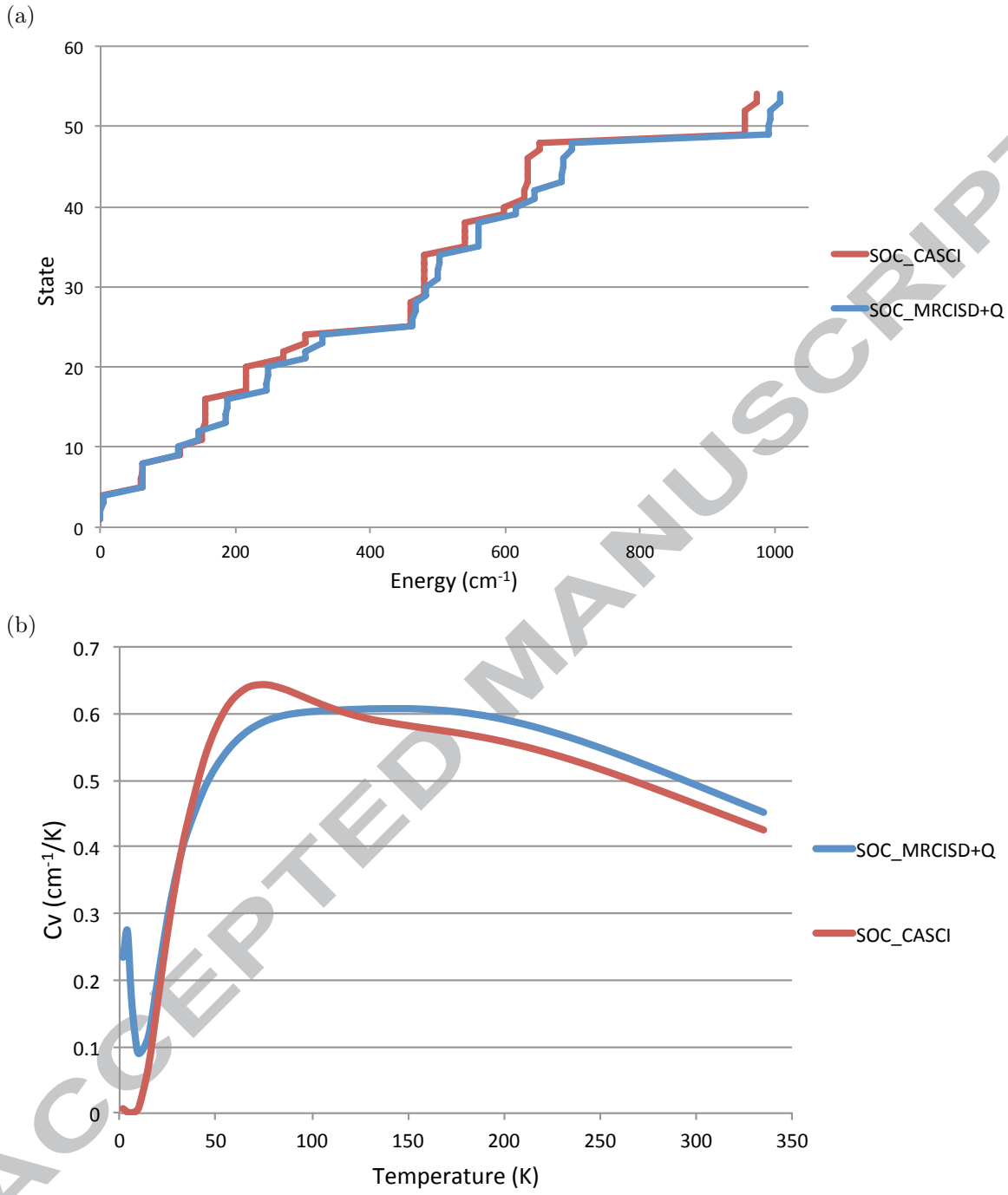

Figure 4: Plots of (a) excitation energies and (b) heat capacity for FArO using the SOC_CASCI and SOC_MRCISD+Q.

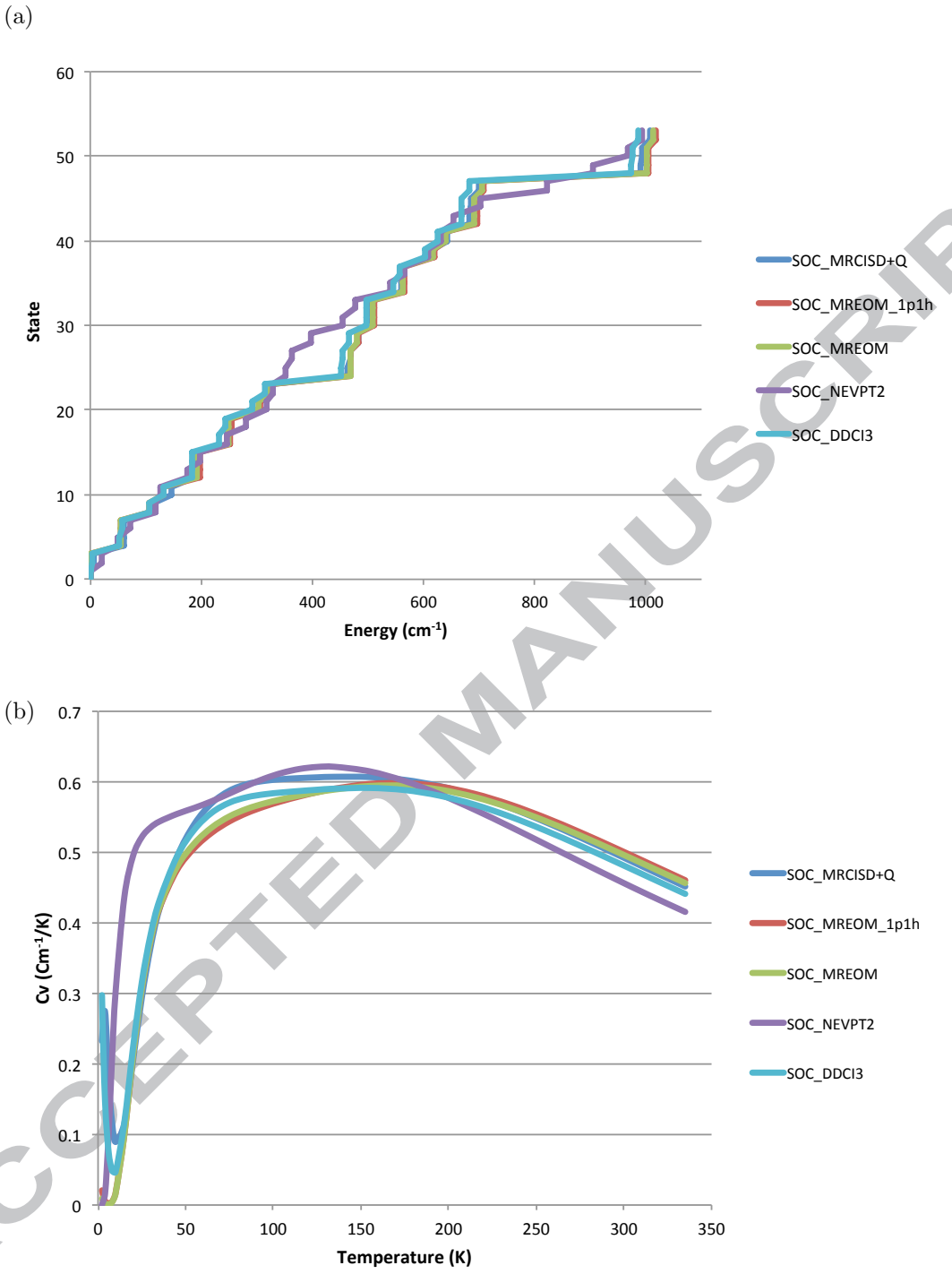

Figure 5: Plots of (a) excitation energies and (b) heat capacity for FArO using the SOC_MRCISD+Q, SOC_MREOM, SOC_MREOM_1p1h, SOC_NEVPT2 and SOC_DDCI3.

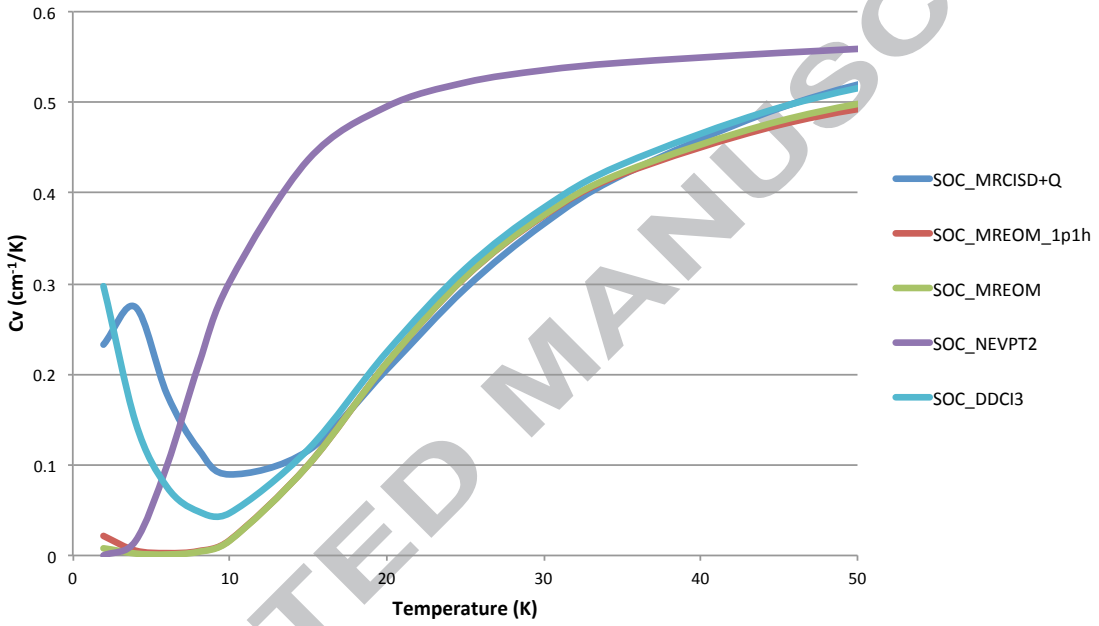

Figure 6: Plot of heat capacity for FArO using the SOC_MRCISD+Q, SOC_MREOM, SOC_MREOM_1p1h, SOC_NEVPT2 and SOC_DDCI3 at low temperature range.

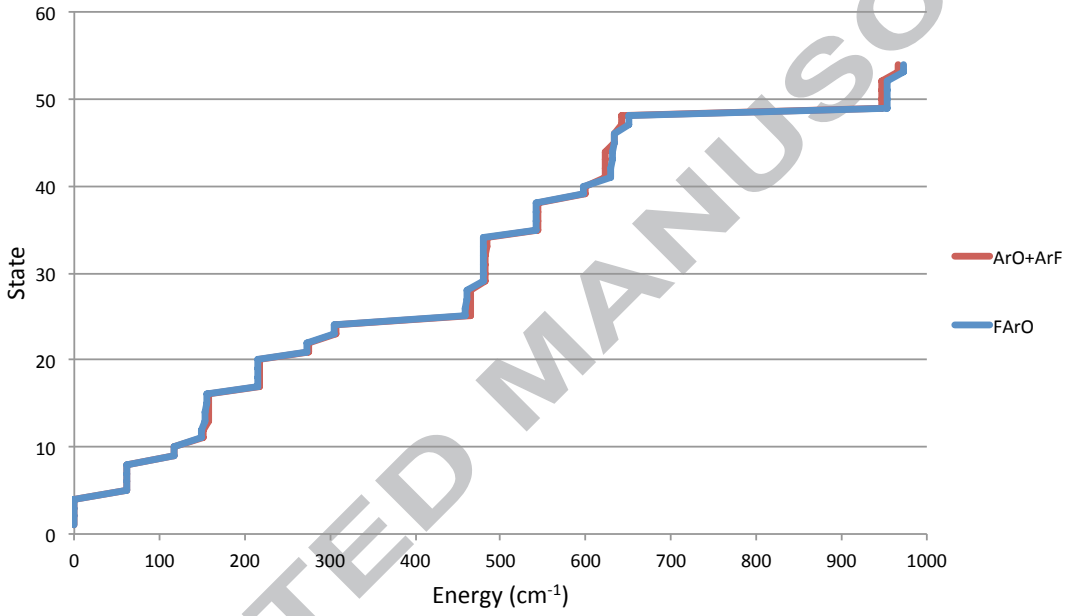

Figure 7: The excitation energies curve of interacting molecule (FArO) and non-interacting molecules (ArF+ArO) using the SOC_CASCI.

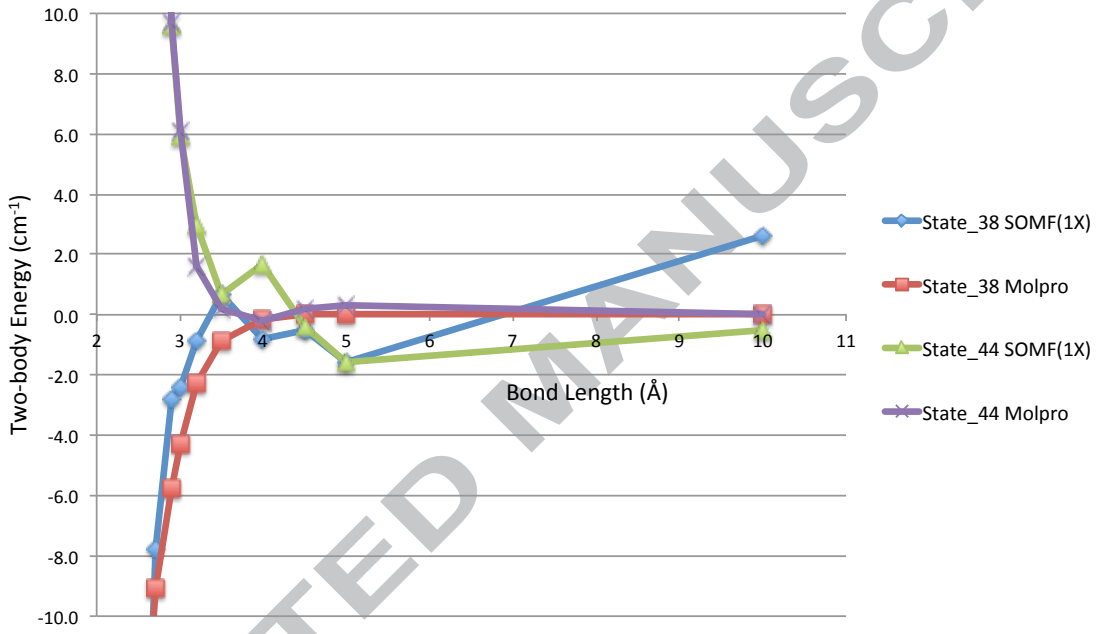

Figure 8: Two-body energies for FArO using default SOC_CASCI in Molpro and ORCA for states 38 and 44.

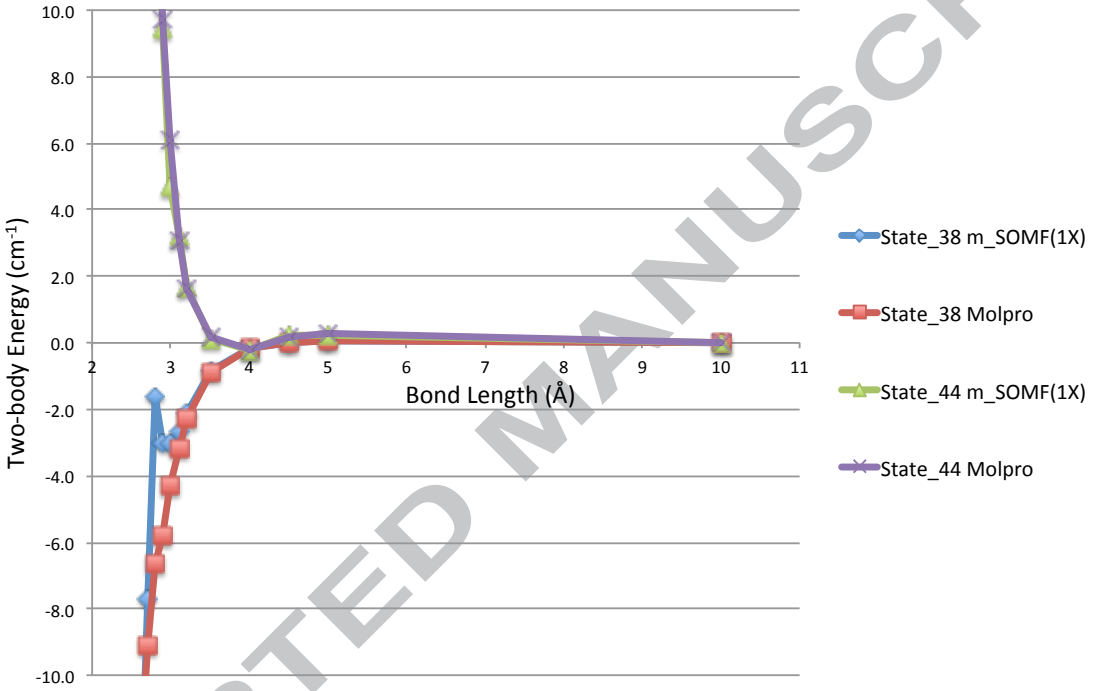

Figure 9: Two-body energies for FArO using default SOC_CASCI in Molpro and m_SOMF(1X) in ORCA for states 38 and 44.

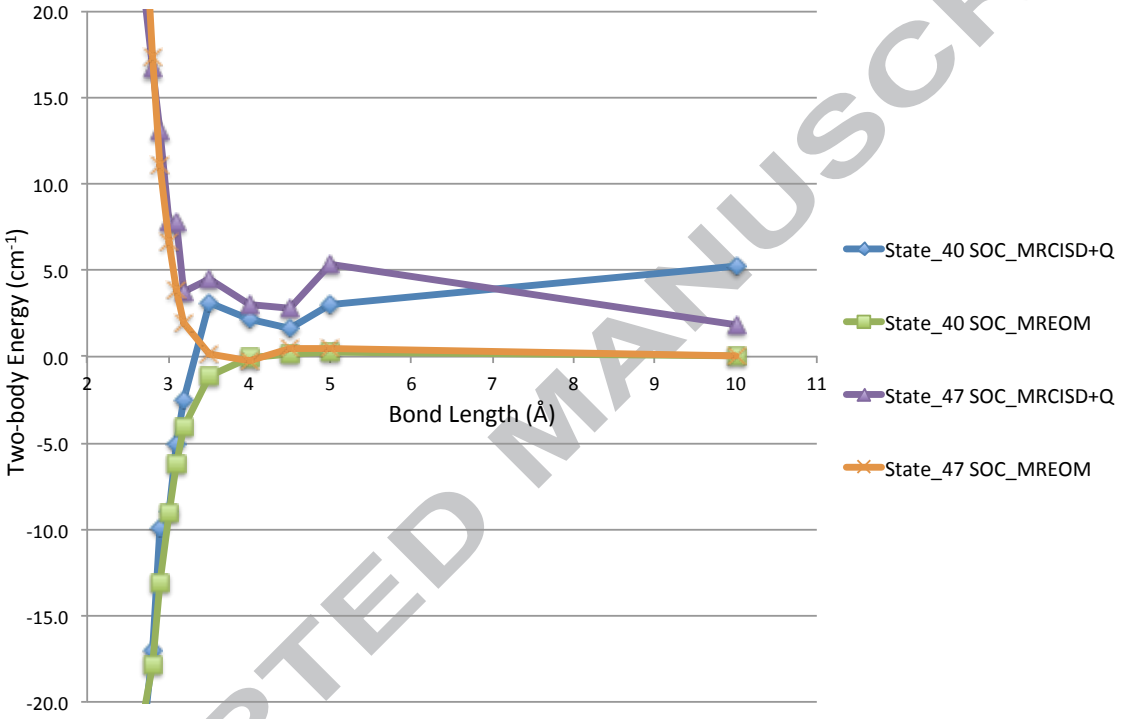

Figure 10: Two-body energies for FArO using the SOC_MRCISD+Q and SOC_MREOM for states 40 and 47.

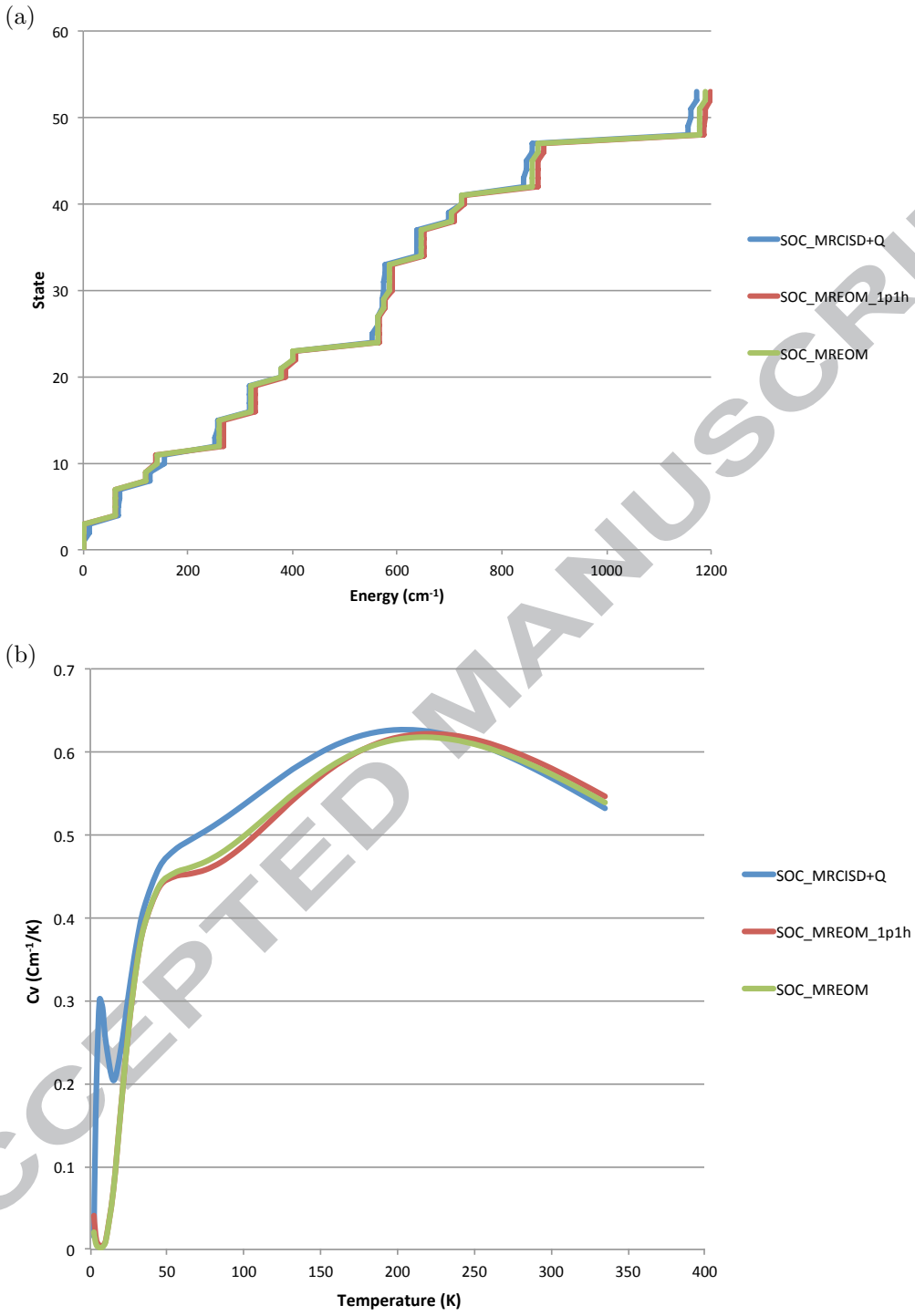

Figure 11: Plots of (a) excitation energies and (b) heat capacity for FArO using the SOC_MRCISD+Q, SOC_MREOM and SOC_MREOM_1p1h using cc-pVTZ basis set.

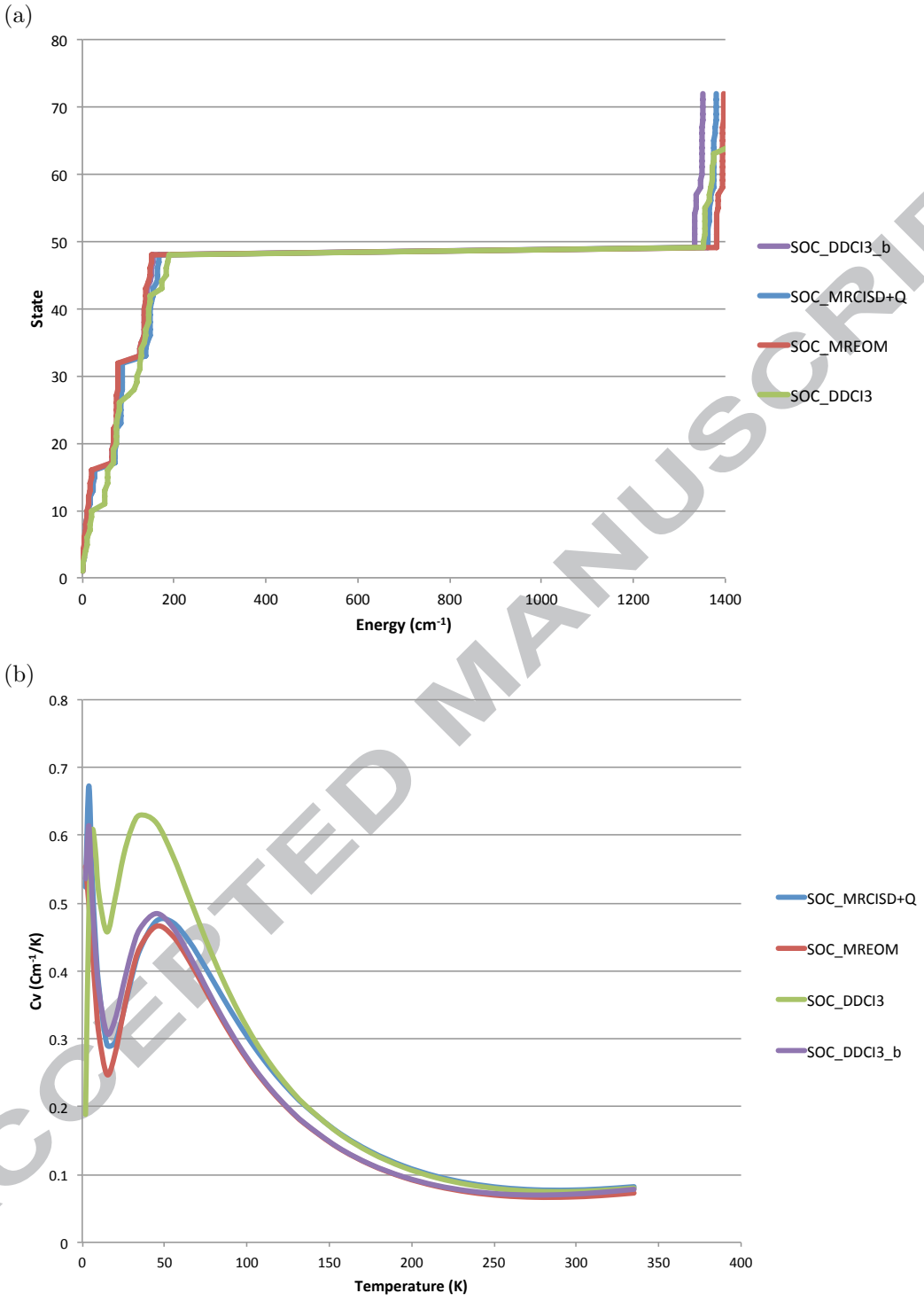

Figure 12: Plots of (a) excitation energies and (b) heat capacity for NArOH using the SOC_MRCISD+Q, SOC_MREOM, SOC_DDCI3 and SOC_DDCI3_b.

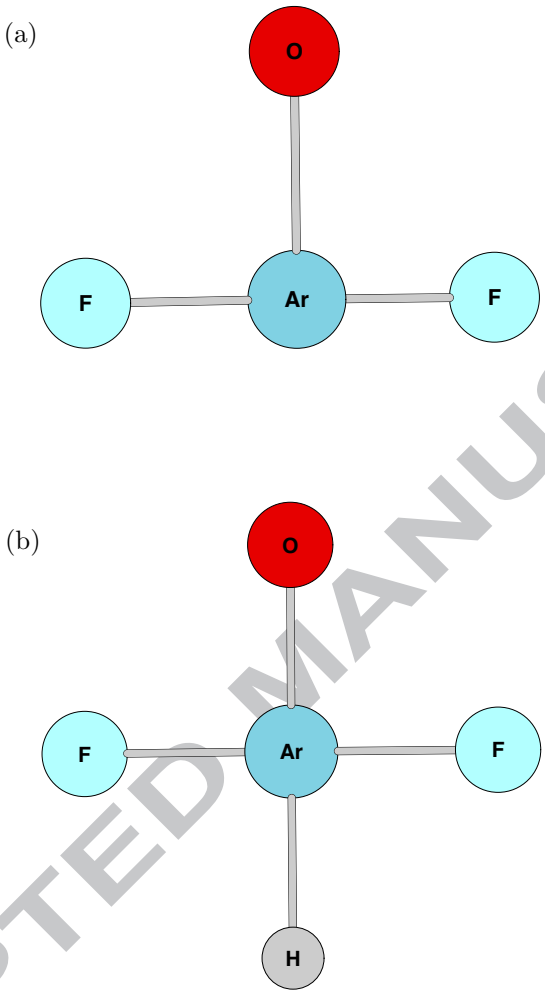

Figure 13: The geometric structure of (a) FArOF and (b) FArOFH molecules. All bond lengths are identical. All bond angles are 90°.

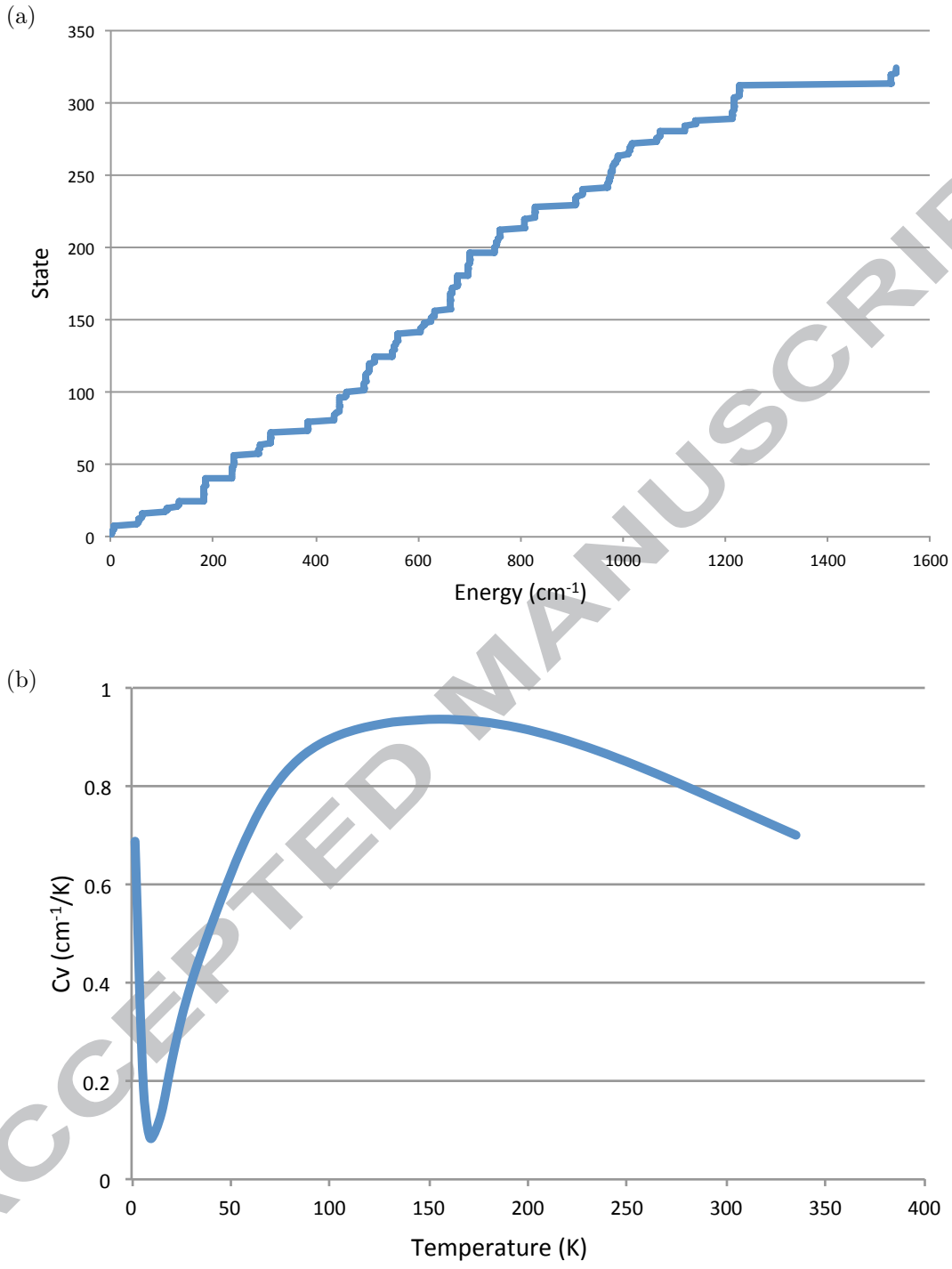

Figure 14: Plots of (a) excitation energies and (b) heat capacity for FArOF using the SOC_MREOM. R = 2.9 Å.

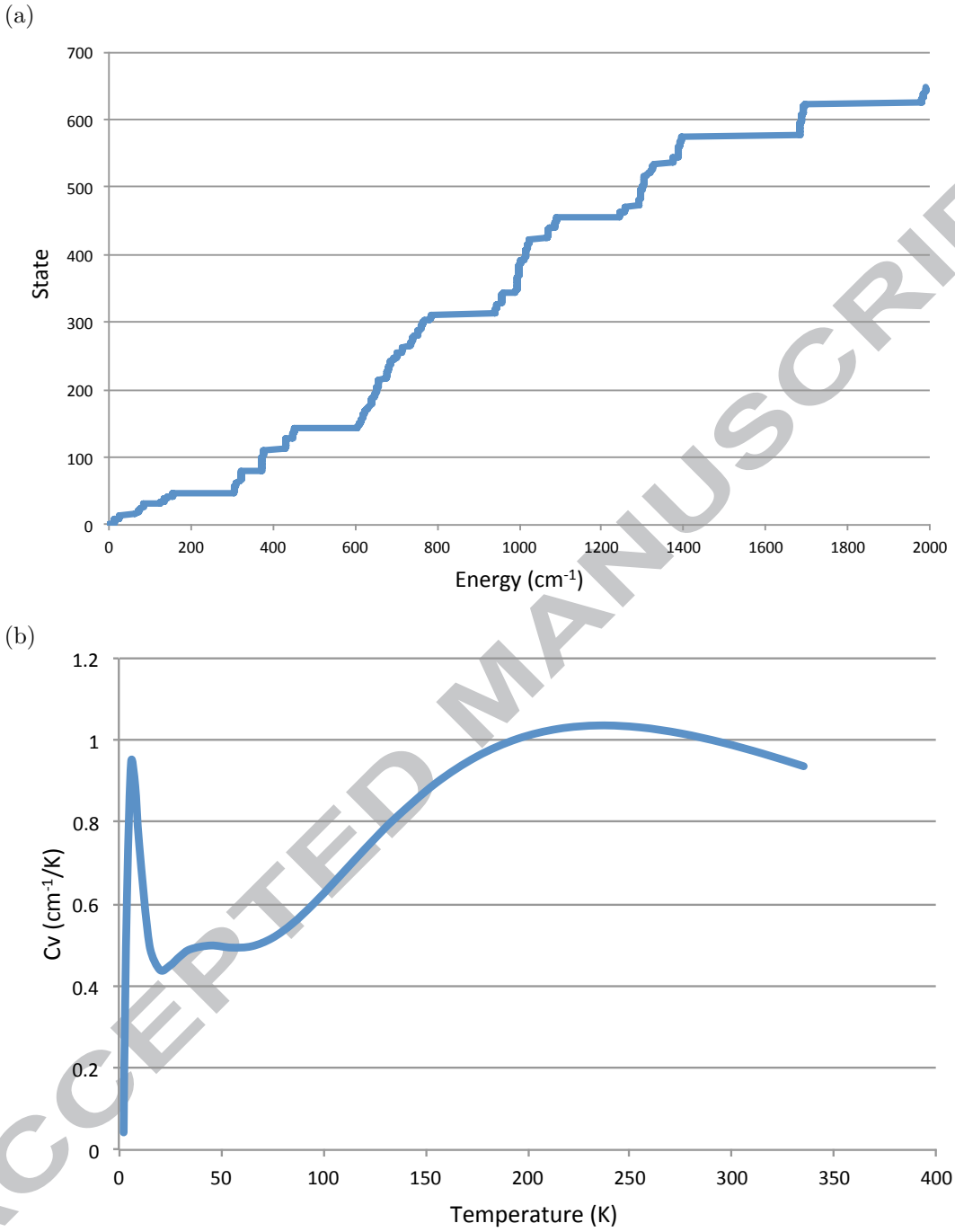

Figure 15: Plots of (a) excitation energies and (b) heat capacity for FArOFH using the SOC_MREOM. R = 2.8 Å.

References

[1] J. Coey, Magnetism in future, J. Magn. Magn. Mater. 226 (2001) 2107–2112.

[2] J. P. Malrieu, R. Caballol, C. J. Calzado, C. De Graaf, N. Guihery, Magnetic interactions in molecules and highly correlated materials: Physical content, analytical derivation, and rigorous extraction of magnetic hamiltonians, Chem. Rev. 114 (1) (2013) 429–492.

[3] C. Bloch, Sur la théorie des perturbations des états liés, Nucl. Phys. 6 (1958) 329–347.

[4] J. des Cloizeaux, Extension d'une formule de lagrange à des problèmes de valeurs propres, Nucl. Phys. 20 (1960) 321–346.

[5] R. Maurice, R. Bastardis, C. d. Graaf, N. Suaud, T. Mallah, N. Guihery, Universal theoretical approach to extract anisotropic spin hamiltonians, J. Chem. Theory Comput. 5 (11) (2009) 2977–2984.

[6] Z. Tabookht, X. López, C. De Graaf, N. Guihéry, N. Suaud, N. Benamor, Rationalization of the behavior of m2 (ch3cs2) 4i (m= ni, pt) chains at room temperature from periodic density functional theory and ab initio cluster calculations, J. Comput. Chem. 33 (21) (2012) 1748–1761.

[7] C. de Graaf, R. Broer, Magnetic Interactions in Molecules and Solids, Springer, Switzerland, 2016.

[8] A. Ginsberg, Magnetic exchange in transition metal complexes. 12. calculation of cluster exchange coupling constants with the x. alpha.-scattered wave method, J. Am. Chem. Soc. 102 (1) (1980) 111–117.

[9] L. Noodleman, Valence bond description of antiferromagnetic coupling in transition metal dimers, J. Chem. Phys. 74 (10) (1981) 5737–5743.

[10] I. de PR Moreira, F. Illas, A unified view of the theoretical description of magnetic coupling in molecular chemistry and solid state physics, Phys. Chem. Chem. Phys. 8 (14) (2006) 1645–1659.

[11] A. Bencini, Some considerations on the proper use of computational tools in transition metal chemistry, Inorg. Chim. Acta. 361 (14) (2008) 3820–3831.

[12] A. Bencini, F. Totti, A few comments on the application of density functional theory to the calculation of the magnetic structure of oligo-nuclear transition metal clusters, J. Chem. Theory Comput. 5 (1) (2008) 144–154.

[13] F. Neese, Prediction of molecular properties and molecular spectroscopy with density functional theory: From fundamental theory to exchange-coupling, Coord. Chem. Rev. 253 (5) (2009) 526–563.

[14] A. J. Cohen, P. Mori-Sánchez, W. Yang, Challenges for density functional theory, Chem. Rev. 112 (1) (2011) 289–320.

[15] J. Miralles, O. Castell, R. Caballol, J.-P. Malrieu, Specific ci calculation of energy differences: Transition energies and bond energies, Chem. Phys. 172 (1) (1993) 33–43.

[16] K. Handrick, J. P. Malrieu, O. Castell, General strategy for the ab initio calculation of exchange coupling in polynuclear complexes, J. Chem. Phys. 101 (3) (1994) 2205–2212.

[17] V. Barone, I. Cacelli, A. Ferretti, M. Girlanda, Toward an effective yet reliable many-body computation of magnetic couplings in bisnitronyl nitroxide biradicals, J. Chem. Phys. 128 (17) (2008) 174303.

[18] V. Barone, I. Cacelli, A. Ferretti, G. Prampolini, Modified virtual orbitals for ci calculations of energy splitting in organic diradicals, Phys. Chem. Chem. Phys. 11 (20) (2009) 3854–3860.

[19] H.-J. Werner, P. J. Knowles, An efficient internally contracted multiconfiguration–reference configuration interaction method, J. Chem. Phys. 89 (9) (1988) 5803–5814.

[20] K. Shamasundar, G. Knizia, H.-J. Werner, A new internally contracted multi-reference configuration interaction method, J. Chem. Phys. 135 (5) (2011) 054101.

[21] D. Datta, M. Nooijen, Multireference equation-of-motion coupled cluster theory, J. Chem. Phys. 137 (20) (2012) 204107.

[22] O. Demel, D. Datta, M. Nooijen, Additional global internal contraction in variations of multireference equation of motion coupled cluster theory, J. Chem. Phys. 138 (13) (2013) 134108.

[23] M. Nooijen, L. M. Huntington, O. Demel, D. Datta, L. Kong, K. Shamasundar, V. Lotrich, F. Neese, Communication: Multireference equation of motion coupled cluster: A transform and diagonalize approach to electronic structure, J. Chem. Phys. 140 (8) (2014) 081102–081102.

[24] B. O. Roos, Taylor, P. R, Si, P. EM, A complete active space scf method (casscf) using a density matrix formulated super-ci approach, Chem. Phys. 48 (2) (1980) 157–173.

[25] L. M. Huntington, M. Nooijen, Application of multireference equation of motion coupled-cluster theory to transition metal complexes and an orbital selection scheme for the efficient calculation of excitation energies, J. Chem. Phys. 142 (19) (2015) 194111.

[26] L. M. Huntington, O. Demel, M. Nooijen, Benchmark applications of variations of multireference equation of motion coupled-cluster theory, J. Chem. Theory Comput. 12 (1) (2015) 114–132.

[27] F. Neese, The orca program system, WIREs Comput. Mol. Sci. 2 (1) (2012) 73–78.

[28] F. Neese, Efficient and accurate approximations to the molecular spin-orbit coupling operator and their use in molecular g-tensor calculations, J. Chem. Phys. 122 (3) (2005) 034107.

[29] H. Kramers, L'interaction entre les atomes magnétogènes dans un cristal paramagnétique, Physica 1 (1-6) (1934) 182–192.

[30] P. Anderson, Antiferromagnetism. theory of superexchange interaction, Phys. Rev. 79 (2) (1950) 350.

[31] J. Kanamori, Superexchange interaction and symmetry properties of electron orbitals, J. Phys. Chem. Solids 10 (2) (1959) 87–98.

[32] H.-J. Werner, P. J. Knowles, G. Knizia, F. R. Manby, M. Schütz, Molpro: A general-purpose quantum chemistry program package, WIREs Comput. Mol. Sci. 2 (2) (2012) 242–253.

[33] D. Mukherjee, Normal ordering and a wick-like reduction theorem for fermions with respect to a multi-determinantal reference state, Chem. Phys. Lett. 274 (5-6) (1997) 561–566.

[34] W. Kutzelnigg, D. Mukherjee, Normal order and extended wick theorem for a multiconfiguration reference wave function, J. Chem. Phys. 107 (2) (1997) 432–449.

[35] L. Kong, M. Nooijen, D. Mukherjee, An algebraic proof of generalized wick theorem, J. Chem. Phys. 132 (23) (2010) 234107.

[36] D. Datta, L. Kong, M. Nooijen, A state-specific partially internally contracted multireference coupled cluster approach, J. Chem. Phys. 134 (21) (2011) 214116.

[37] F. Neese, T. Petrenko, D. Ganyushin, G. Olbrich, Advanced aspects of ab initio theoretical optical spectroscopy of transition metal complexes: Multiplets, spin-orbit coupling and resonance raman intensities, Coord. Chem. Rev. 251 (3) (2007) 288–327.

[38] D. Ganyushin, F. Neese, First-principles calculations of zero-field splitting parameters, J. Chem. Phys. 125 (2) (2006) 024103.

[39] B. A. Hess, C. M. Marian, U. Wahlgren, O. Gropen, A mean-field spin-orbit method applicable to correlated wavefunctions, Chem. Phys. Lett. 251 (5-6) (1996) 365–371.

[40] Z. Liu, L. M. Huntington, M. Nooijen, Application of the multireference equation of motion coupled cluster method, including spin–orbit coupling, to the atomic spectra of cr, mn, fe and co, Mol. Phys. 113 (19-20) (2015) 2999–3013.

[41] S. R. Langhoff, E. R. Davidson, Configuration interaction calculations on the nitrogen molecule, Int. J. Quantum Chem. 8 (1) (1974) 61–72.

[42] W. Butscher, S.-K. Shih, R. J. Buenker, S. D. Peyerimhoff, Configuration interaction calculations for the n2 molecule and its three lowest dissociation limits, Chem. Phys. Lett. 52 (3) (1977) 457–462.

[43] C. Angeli, R. Cimiraglia, S. Evangelisti, T. Leininger, J.-P. Malrieu, Introduction of n-electron valence states for multireference perturbation theory, J. Chem. Phys. 114 (23) (2001) 10252–10264.

[44] C. Angeli, R. Cimiraglia, J.-P. Malrieu, n-electron valence state perturbation theory: A spinless formulation and an efficient implementation of the strongly contracted and of the partially contracted variants, J. Chem. Phys. 117 (20) (2002) 9138–9153.

[45] T. H. Dunning Jr, Gaussian basis sets for use in correlated molecular calculations. i. the atoms boron through neon and hydrogen, J. Chem. Phys. 90 (2) (1989) 1007–1023.

[46] D. E. Woon, T. H. Dunning Jr, Gaussian basis sets for use in correlated molecular calculations. iii. the atoms aluminum through argon, J. Chem. Phys. 98 (2) (1993) 1358–1371.

Highlights:

- MREOM calculations including spin-orbit coupling provide highly accurate results for magnetic model systems.
- A modification of spin-orbit mean-field calculation in ORCA is needed to yield size-consistent results.
- MREOM calculations provide a computationally efficient strategy to magnetic model systems.
- A large number of low-lying electronic states (up to 648 states) are obtained.

Graphical Abstract

Heat Capacity Plot for NArOH